crystals

MDPI

Article

Case Study of High-Throughput Drug Screening and Remote Data Collection for SARS-CoV-2 Main Protease by Using Serial Femtosecond X-ray Crystallography

Omur Guven [1,†], Mehmet Gul [1,†], Esra Ayan [1], J Austin Johnson [1], Baris Cakilkaya [1], Gozde Usta [1], Fatma Betul Ertem [1], Nurettin Tokay [1], Busra Yuksel [1], Oktay Gocenler [1], Cengizhan Buyukdag [1], Sabine Botha [2,3], Gihan Ketawala [2,3], Zhen Su [4,5], Brandon Hayes [4], Frederic Poitevin [4], Alexander Batyuk [4], Chun Hong Yoon [4], Christopher Kupitz [4], Serdar Durdagi [6], Raymond G. Sierra [4] and Hasan DeMirci [1,7,8,*]

1 Department of Molecular Biology and Genetics, Koc University, Istanbul 34450, Turkey; oguven@ku.edu.tr (O.G.); mgul21@ku.edu.tr (M.G.); esraayan20@ku.edu.tr (E.A.); jjohnson19@ku.edu.tr (J.A.J.); bcakilkaya14@ku.edu.tr (B.C.); gusta21@ku.edu.tr (G.U.); fertem19@ku.edu.tr (F.B.E.); ntokay21@ku.edu.tr (N.T.); byuksel20@ku.edu.tr (B.Y.); ogocenler18@ku.edu.tr (O.G.); cbuyukdag19@ku.edu.tr (C.B.)
2 Department of Physics, Arizona State University, Tempe, AZ 85287, USA; sbotha@asu.edu (S.B.); Gihan.Ketawala@asu.edu (G.K.)
3 Biodesign Center for Applied Structural Discovery, Arizona State University, Tempe, AZ 85287, USA
4 Linac Coherent Light Source, SLAC National Accelerator Laboratory, 2575 Sand Hill Rd., Menlo Park, CA 94025, USA; zhensu@stanford.edu (Z.S.); bhayes@slac.stanford.edu (B.H.); fpoitevi@slac.stanford.edu (F.P.); batyuk@slac.stanford.edu (A.B.); chuckyoon@stanford.edu (C.H.Y.); ckupitz@slac.stanford.edu (C.K.); rsierra@slac.stanford.edu (R.G.S.)
5 Department of Applied Physics, Stanford University, Stanford, CA 94305, USA
6 Computational Biology and Molecular Simulations Laboratory, Department of Biophysics, School of Medicine, Bahcesehir University, Istanbul 34734, Turkey; serdar.durdagi@med.bau.edu.tr
7 Koc University Isbank Center for Infectious Diseases (KUISCID), Koc University, Istanbul 34010, Turkey
8 Stanford PULSE Institute, SLAC National Laboratory, Menlo Park, CA 94025, USA
* Correspondence: hdemirci@ku.edu.tr
† Equal contribution.

check for updates

Citation: Guven, O.; Gul, M.; Ayan, E.; Johnson, J.A.; Cakilkaya, B.; Usta, G.; Ertem, F.B.; Tokay, N.; Yuksel, B.; Gocenler, O.; et al. Case Study of High-Throughput Drug Screening and Remote Data Collection for SARS-CoV-2 Main Protease by Using Serial Femtosecond X-ray Crystallography. *Crystals* **2021**, *11*, 1579. https://doi.org/10.3390/cryst11121579

Academic Editors: Marc Messerschmidt, Jeney Wierman and José Manuel Martín-García

Received: 17 October 2021
Accepted: 28 November 2021
Published: 17 December 2021

Publisher's Note: MDPI stays neutral with regard to jurisdictional claims in published maps and institutional affiliations.

Copyright: © 2021 by the authors. Licensee MDPI, Basel, Switzerland. This article is an open access article distributed under the terms and conditions of the Creative Commons Attribution (CC BY) license (https://creativecommons.org/licenses/by/4.0/).

Abstract: Since early 2020, COVID-19 has grown to affect the lives of billions globally. A worldwide investigation has been ongoing for characterizing the virus and also for finding an effective drug and developing vaccines. As time has been of the essence, a crucial part of this research has been drug repurposing; therefore, confirmation of in silico drug screening studies have been carried out for this purpose. Here we demonstrated the possibility of screening a variety of drugs efficiently by leveraging a high data collection rate of 120 images/second with the new low-noise, high dynamic range ePix10k2M Pixel Array Detector installed at the Macromolecular Femtosecond Crystallography (MFX) instrument at the Linac Coherent Light Source (LCLS). The X-ray Free-Electron Laser (XFEL) is used for remote high-throughput data collection for drug repurposing of the main protease (Mpro) of SARS-CoV-2 at ambient temperature with mitigated X-ray radiation damage. We obtained multiple structures soaked with nine drug candidate molecules in two crystal forms. Although our drug binding attempts failed, we successfully established a high-throughput Serial Femtosecond X-ray crystallographic (SFX) data collection protocol.

Keywords: SARS-CoV-2; main protease; serial femtosecond crystallography; high-throughput drug screening

1. Introduction

Emerging infectious diseases (EID) rapidly spread in a population [1]. Acquired immune deficiency syndrome (AIDS) [2], Lyme disease [3], H1N1 influenza [4], severe acute respiratory syndrome (SARS) [5], Zika, and Middle East respiratory syndrome

(MERS) are among the recent outbreaks. Despite technological advances in healthcare, EIDs remain a very significant threat to global health [6]. In order to prevent and control the spread of such diseases, high-throughput approaches can play an essential role in drug repurposing and development.

SARS-CoV-2, like other coronaviruses, generates numerous polyproteins that must be processed into functional, unique proteins, such as nonstructural proteins required for viral replication [7]. SARS-CoV-2 genome encodes two proteases: papain-like cysteine protease (PLpro) and chymotrypsin-like cysteine protease, also called 3C-like protease (3CLpro) [8]. For the SARS-CoV-2 lifecycle, 3CLpro is necessary. This main protease 3CLpro (referred to as Mpro hereafter) is responsible for functional protein maturation and can be an attractive primary antiviral target [9]. Besides functional importance, targeting proteases, such as Mpro, is a common approach for combating viral infections because those proteins are highly conserved between species [10]. For instance, several Mpro drug targeting studies for SARS-CoV, MERS-CoV, and other viruses have been performed [11,12]; those efforts made the drug repurposing and design studies for SARS-CoV-2 Mpro possible due to a conserved active site and proteolytic activity [13]. Mpro is enzymatically active in the dimeric form, and its Cys-His catalytic dyad provides sequence-specific cleavage after Gln residues of polyproteins [10]. However, this conserved protein has no homologs or similar cleavage sites for proteases found in the human proteome, making it an ideal potential drug repurposing and screening target. Thus, drugs targeting Mpro are expected to have less or no side effects and toxicity while still acting as a broad-spectrum antiviral agent [14,15].

Drug-target complex structures determined at an atomic resolution are regularly used for drug repurposing [13]. X-ray Free-Electron Lasers (XFELs) are premier light sources for structure determination as they provide structures with mitigated radiation damage at ambient (near-physiological) temperatures. With high energy beams and 10–100 femtosecond (fs) pulse length, XFELs can help us to determine electronic states and molecular dynamics information that is invaluable for drug-repurposing studies. The comparatively brighter, short X-ray pulses, and the collection of diffraction data from exceedingly small (sub-micrometer) protein crystals make the use of hard XFELs attractive [16].

Previous structural studies conducted at the Linac Coherent Light Source (LCLS) facility have obtained two Mpro structures of SARS-CoV-2 with mitigated electron radiation damage, paving the way for potential drug repurposing studies for the treatment of COVID-19 [17]. High-throughput screening (HTS) is one of the methods used to discover small lead molecules and allowed development of new and higher quality drug candidates [18]. Various high-throughput screening studies with Nuclear Magnetic Resonance (NMR) spectroscopy are available in the literature. The most striking study was the high-throughput screening for the discovery of antiviral drugs against Ebola [19]. A similar study focuses on fragment screening for the DC-SIGN (Dendritic Cell-Specific Intercellular adhesion molecule-3-Grabbing Non-integrin) receptor. It is targeted by pathogens such as HIV, Ebola virus, and *Mycobacterium tuberculosis*. Within the scope of the study, five potential secondary target drug binding sites were identified [20]. In a recent study conducted at the Diamond Light Source, high-throughput crystallographic fragment screening was performed for SARS-CoV-2′s Nsp3 Mac 1 protein, which plays an essential role for viral replication. As a result, they identified numerous compounds that can be drug candidates against COVID-19 [21].

In this study, we report high-throughput X-ray diffraction data collection results for potential drug repurposing. Fifteen SARS-CoV-2 Mpro SFX structures were determined at the Macromolecular Femtosecond Crystallography (MFX) instrument of the LCLS at ambient temperature. XFELs provide micro-focused, ultrabright, and ultrafast X-ray pulses to probe micro- and nanocrystals in a serial fashion by obtaining individual snapshots and capturing Bragg reflection from exceedingly small crystals. It eliminates larger crystal growth requirements and simplifies optimization processes in batch mode, thus enabling it to work with multiple crystal forms and space groups. In a previous study, we obtained structures of SARS-CoV-2 Mpro at ambient temperature and verified the dynamic regions of

the active site through the SFX approach [17]. This suggests immense potential by providing critical information for future high-throughput data collection for drug repurposing and computational modeling studies.

COVID-19 pandemic has shown us the importance of drug design/repurposing for infectious diseases and our workflow is an ideal suited for future drug repurposing and screening studies. The method is fast, effective, and physiologically relevant since the structures are obtained at ambient temperature.

2. Materials and Methods

2.1. Gene Construct Design, Protein Expression, and Purification

Two Mpro gene constructs were designed, expressed, and purified as stated in [17]. Two Mpro gene constructs were ordered from Genscript (Piscatway, NJ, USA), USA in a pET28a(+) *Escherichia coli* expression vector. One of our constructs had an N-terminus hexahistidine-tag with a native Mpro cleavage site and a C-terminal PreScission™ cut site. After the protease cuts, Mpro is left with native N- and C- terminals; this construct is referred to as the "native construct". The other construct had an N-terminal thrombin cut site that leaves an additional four residues upon cleavage (GSHM); hence, it is called the "modified construct". Bacterial transformations were performed on a chemically competent *Escherichia coli* BL21 Rosetta-2 strain for both constructs. Transformed cells were grown in 12 L LB-Miller media supplemented with 50 µL/mL kanamycin and 35 µL/mL chloramphenicol antibiotics at 37 °C. When the OD600 reached ~1.0, isopropyl β-D-1-thiogalactopyranoside (IPTG) induction was done with a final concentration of 0.4 mM IPTG for protein production. Cells were harvested at 3500 rpm for 20 min at 4 °C by using Beckman Allegra 15R desktop centrifuge. Supernatant was discarded and cell pellets were stored at −80 °C until protein purification. The pellet was dissolved in a lysis buffer containing 50 mM Tris-HCl (pH 7.5), 300 mM NaCl and 5% *v*/*v* glycerol supplemented with 0.01% Triton X-100 by sonicating the solution (Branson W250 sonifier, Brookfield, CT, USA). Cell lysate was ultracentrifuged (The Beckman Optima™ L-80 XP Ultracentrifuge) at 40,000 rpm for 30 min at 4 °C with a Ti45 rotor (Beckman, Brea, CA, USA). Mpro-containing supernatant was applied to an immobilized metal affinity chromatography (IMAC) column by using a Ni-NTA agarose resin (QIAGEN, Hilden, Germany) with a constant flow rate of 2 mL/min. The column was washed with a loading buffer that contains 20 mM Tris-HAc (pH 7.5), 150 mM NaCl, and 5 mM Imidazole to remove non-specific bindings. To elute the Mpro, 20 mM Tris-HAc (pH 7.5), 150 mM NaCl, 250 mM Imidazole elution buffer was applied, and 35 mL of elute was collected. Elute was dialyzed against 20 mM Tris-HAc (pH 7.5), 150 mM NaCl overnight in a 3 kDa cut-off dialysis membrane to remove the excess Imidazole. For the native construct, 3C protease (PreScission protease, GenScript, Piscatway, NJ, USA) was used in a 1:100 stoichiometric molar ratio to cleave the hexahistidine-tag. For the modified Mpro construct, thrombin protease (Sigma, St. Louis, MO, USA) was used in a 1:100 stoichiometric molar ratio to cut off the hexahistidine from the protein. After overnight incubation with proteases at 4 °C, elute was applied to reverse Ni-NTA chromatography to purify the untagged protein from the remaining part of the affinity tag in the solution. Mpro proteins were concentrated to 25 mg/mL by Millipore's ultrafiltration columns and a final concentration of 1 mM DTT was added and stored at −80 °C.

2.2. Crystallization of Protein with Drug by Using Soaking Method

For protein crystallization, high-throughput sitting drop microbatch under paraffin oil screening was performed under paraffin oil. Purified protein with 25 mg/mL concentration was mixed with sparse matrix crystallization screening conditions in a 1:1 volumetric ratio by using 72 well Terasaki crystallization plates (Greiner Bio-One, Kremsmünster, Austria). The mixture was sealed with 100% paraffin oil to slow down the vapor diffusion (Tekkim Kimya, Istanbul, Turkey) and crystallization plates are stored at ambient temperature. The best crystals for the native construct were obtained from Pact Premier™ crystallization screen 1 condition #39 (0.1 M MMT pH 6.0, 25% *w*/*v* PEG 1500) (Molecular Dimensions,

Maumee, OH, USA). For the modified construct, crystals were obtained from Crystal Screen™ crystallization screen condition #22 (0.2 M Sodium acetate trihydrate, 0.1 M Tris pH 8.5, 30% *w*/*v* PEG 4000) (Hampton Research, Aliso Viejo, CA, USA). Successful crystal conditions were replicated at a larger scale where 10 mL of the protein sample was mixed with 10 mL of the referred commercial crystallization conditions. After crystals of size 1–5 µm × 5–10 µm × 10–20 µm reached, they were soaked with 100 µg/mL of drug solution by mixing the drug solutions into protein crystal solution for both constructs. Promising drug candidates were chosen by intensive literature search: Lopinavir [22], Rosuvastatin and Atorvastatin [23], Adefovir [24], Umifenovir [25], Empagliflozin [26], Ebselen [17], and Montelukast [27,28].

2.3. Transport of Microcrystals

Crystals were transferred into screw-top plastic cryovials (Wuxi NEST biotechnology, Wuxi, China cat#607001). The cryovials were loosely wrapped with Kimwipes (Kimberly-Clark, Irving, TX, USA) to absorb mechanical shocks during the transport from Istanbul, Turkey to Menlo Park, CA, USA. These cryovials were placed inside larger screw-top glass vials. The glass vials were covered with extra layers of cotton (Ipek, Istanbul, Turkey) and placed within a Ziploc™ bag (SC Johnson, Racine, WI, USA) for further mechanical shock absorption and providing additional thermal insulation. For further thermal insulation, the Ziploc™ bags were placed in a styrofoam box filled with ~1 kg of cotton during transportation. The styrofoam box was tightly closed and covered with an additional 1 cm thick layer of cotton, duct-taped all around to prevent thermal fluctuations during international transport.

2.4. Injection of Microcrystals

The sample reservoir, which has a volume of 1.6 mL, was filled with soaked crystal slurries in their unmodified mother liquor. To utilize the electrospinning method, a standard Microfluidic Electrokinetic Sample Holder (MESH) was used for sample injection, allowing us to collect full datasets using a reduced amount of sample [29,30]. The sample capillary consists of a 200 µm ID × 360 µm OD × 1.0 m long capillary made of fused silica. The voltage applied to the sample fluid was 2500–3000 V, and the counter electrode was grounded. The sample flow rate was between 2.5 and 8 µL/min in general.

2.5. Data Collection at LCLS

The SFX experiments with microcrystals were performed at the MFX instrument at the LCLS (beamtime ID: mfx17318) at the SLAC National Accelerator Laboratory (Menlo Park, CA, USA). An X-ray beam with a vertically polarized pulse of 30–40 fs duration was focused with refractive beryllium compound lenses with a ~6 × 6 µm full width at half maximum beam size. The total pulse energy was 0.8 mJ, with 9.8 keV (1.25 Å) photon energy, 10^{12} photons per pulse flux and a 120 Hz repetition rate. *OM monitor* version 1.0 [31] and *PSOCAKE* version 1.0.8 [32,33] were used to determine the initial diffraction geometry, monitor the crystal hit rates, and analyze the gain switching modes of the epix10k 2-megapixel (ePix10k2M) detector [34]. The detector frames were collected continuously from Mpro microcrystals, and the total number of frames collected per datasets ranged from 192,352 to 1,465,292 (Table 1). Total run times were between 36 min and 5 h 20 min with the effective run times ranging from 36 min to 4 h 20 min (Table 1). The ePix10k2M detector was used in dynamic gain mode activated. During the data collection the MESH injector system had no blockages. The total number of frames with more than 30 Bragg reflections and a signal-to-noise ratio larger than 4.5 were considered as a hit and their numbers were ranged from 5274 to 45,521 per dataset (Table 1). The distance for the detector was 118 mm that has a 2.1 Å achievable resolution on the edges and 1.64 Å in the corners. All the relevant information for the data collection process is further summarized in Table 1.

Table 1. Serial femtosecond X-ray data collection statistics.

Sample ID	PDB ID	Total Run Time	Effective Run Time	Runs	Run Number	Total Number Frames Collected	Total Number Frames with More Than 30 Bragg Reflections and a Signal to Noise Ratio > 4.5	Hit Rate (%)	Total Number of Crystal Lattices Indexed to the Appropriate Unit Cell	Total Number of Crystal Lattices Merged into the Final SFX Dataset
Mpro3	7VJY	5 h 20 min	4 h 20 min	20–80	60	1,465,292	279,428	19.07	73,605	68,314
Mpro4	7VK3	3 h 28 min	2 h 59 min	82–115	33	1,121,297	182,774	16.3	33,384	67,918
Mpro5	7CWB	2 h 59 min	2 h 52 min	118–144	26	1,163,413	208,839	17.95	168,655	160,510
Mpro6	7VK4	2 h 18 min	2 h 18 min	235–257	22	790,492	229,422	29.02	315,158	313,250
Mpro7	7VK8	1 h 25 min	45 min	176–188	12	327,156	2078	0.63	1177	947
Mpro8	N/A	N/A	N/A	N/A	N/A	N/A	13	N/A	N/A	N/A
Mpro9	7VK1	3 h 04 min	3 h 04 min	145–174	29	1,148,580	51,112	4.45	33,384	30,732
Mpro10	7VK0	2 h 11 min	2 h 11 min	264–291	27	858,742	932,35	10.86	116,315	115,577
Mpro11	7VJZ	2 h 07 min	1 h 57 min	189–213	24	669,237	132,447	19.79	70,272	65,579
Mpro12	7VK5	1 h 30 min	1 h 30 min	292–310	18	609,036	80,383	13.19	120,147	119,430
Mpro13	7VK2	2 h 47 min	2 h 47 min	216–234	18	873,323	180,625	20.68	88,551	81,563
Mpro14	7VJW	1 h 12 min	1 h 12 min	312–234	7	192,352	15,899	8.26	22,470	21,278
Mpro15	N/A	N/A	N/A	N/A	N/A	N/A	0	N/A	N/A	N/A
Mpro16	7CWC	1 h 53 min	1 h 53 min	320–340	20	686,808	214,355	31.21	15,7976	156,512
Mpro17	7VK7	1 h 28 min	1 h 28 min	341–357	16	439,830	86,490	19.66	174,120	173,796
Mpro18	7VJX	1 h 22 min	1 h 22 min	358–372	15	466,014	111,815	23.99	170,214	169,695
Mpro19	7VK6	36 min	36 min	373–375	3	326,781	78,455	24.01	111,145	107,895

2.6. Data Processing

Data processing details were performed as described in the article by Durdagi et al. [17]. The hit findings and detector correction were performed through the *CHEETAH* software version 6.4.1 [35]. All data sets were classified according to the hit finding parameters created using *peakfinder8* [35]. The crystal hits were indexed through *CrystFEL* version 0.9.0 [36] software package and specific indexing algorithms. Indexed reflections integrated and merged through *PARTIALATOR* [37] were obtained as a complete reflection intensity list from *CrystFEL* [36]. These intensities were scaled and trimmed through the *TRUNCATE* [38] program. The indexed patterns were merged as the final dataset.

2.7. Structure Determination

Structure determination was performed as described in the article by Durdagi et al. [17]. The determination of Mpro crystal forms was accomplished by the automated molecular replacement (MR) program *PHASER* version 2.8.3 [39]. For MR phasing of the structures in the space group C121, we used the coordinates of PDB ID: 7CWB [17] as our initial search model. For the structures in the space group $P2_12_12_1$, we used the coordinates of PDB ID: 7CWC [17] as our initial MR search model. We performed our initial rigid-body refinements through the *PHENIX* version 1.19.2 [40] software package. The positions of altered side chains were defined by completing simulated-annealing refinement followed by individual coordinates and TLS parameter refinement. The water molecules and strong difference density positions of the structures were checked using the *COOT* version 0.8.9.2 [41] software. Structural alignments and all figures were generated using the *PyMOL* version 2.5.2 [42] software. The statistics for the structure determination are summarized in Table 2.

Table 2. Data collection and refinement statistics for X-ray crystallography.

Dataset	Mpro3	Mpro4	Mpro5	Mpro6	Mpro7
PDB ID	7VJY	7VK3	7CWB	7VK4	7VK8
Data collection					
Beamline	LCLS (MFX)	LCLS (MFX)	LCLS (MFX)	LCLS (MFX)	LCLS (MFX)
Space group	C121	$P2_12_12_1$	C121	$P2_12_12_1$	C121
Cell dimensions					
a, *b*, *c* (Å)	114.0, 53.5, 45.0	69.3, 104.4, 105.7	114.0, 53.5, 45.0	68.9, 103.9, 105.2	115.3, 55.2, 45.7
α, β, γ (°)	90.0, 102.0, 90.0	90.0, 90.0, 90.0	90.0, 102.0, 90.0	90.0, 90.0, 90.0	90.0, 101.3, 90.0
Resolution (Å) [1]	48.24–1.73 (1.80–1.73) [1]	46.8–2.14 (2.22–2.14) [1]	55.0–1.9 (1.98–1.90) [1]	46.9–2.14 (2.22–2.14) [1]	31.92–2.34 (2.43–2.34) [1]
R_{split}	1.09 (36.1)	1.12 (54.4)	0.63 (0.94)	0.49 (45.2)	5.94 (13.5)
CC1/2	0.998 (0.179)	0.982 (0.089)	0.996 (0.598)	0.998 (0.331)	0.477 (0.194)
$I/\sigma I$	0.25	0.22	0.57	0.23	0.97
CC*	0.997 (0.552)	0.998 (0.405)	0.999 (0.865)	1.000 (0.705)	0.804 (0.410)
Completeness (%)	100.0 (100.0)	100.0 (26.0)	100.0 (100.0)	100.0 (100.0)	99.2 (98.0)
Redundancy	387	1779	825	5066	9.2
Refinement					
Resolution (Å)	48.2–1.9 (1.95–1.90) [1]	46.8–2.22 (2.29–2.22) [1]	34.0–1.9 (1.95–1.90) [1]	46.9–2.1 (2.15–2.10) [1]	31.9–2.4 (2.51–2.40) [1]
No. reflections	21,030 (1359)	42,380 (3277)	21,029 (1359)	44,742 (3028)	11,028 (1197)
R_{work}/R_{free}	0.23/0.28 (0.49/0.52)	0.24/0.28 (0.41/0.43)	0.22/0.26 (0.43/0.49)	0.21/0.23 (0.30/0.34)	0.22/0.25 (0.34/0.41)
No. atoms					
Protein	2427	4710	2447	4675	2435
Ligand/Ion/Water	60	114	113	7	67
B-factors					
Protein	38.59	53.56	42.86	64.78	31.50
Ligand/Ion/Water	38.02	52.13	51.0	32.72	24.57
Coordinate errors	0.39	0.39	0.34	0.29	0.49
R.m.s deviations					

Table 2. *Cont.*

Dataset	Mpro3	Mpro4	Mpro5	Mpro6	Mpro7
Bond lengths (Å)	0.010	0.004	0.007	0.013	0.004
Bond angles (°)	1.183	0.873	0.869	1.567	0.746
Ramachandran plot					
Favored (%)	293 (96.4)	573 (96.3)	294 (96.7)	573 (97.3)	290 (96.4)
Allowed (%)	6 (2.0)	17 (2.9)	9 (3.0)	12 (2.0)	9 (3.0)
Disallowed (%)	5 (1.6)	5 (0.8)	1 (0.3)	4 (0.7)	2 (0.7)
Dataset	**Mpro9**	**Mpro10**	**Mpro11**	**Mpro12**	**Mpro13**
PDB ID	7VK1	7VK0	7VJZ	7VK5	7VK2
Data collection [1]					
Beamline	LCLS (MFX)	LCLS (MFX)	LCLS (MFX)	LCLS (MFX)	LCLS (MFX)
Space group	C121	P212121	C121	P212121	C121
Cell dimensions					
a, *b*, *c* (Å)	114.0, 53.5, 45.0	69.2, 104.3, 105.7	115.7, 55.2, 45.6	69.2, 104.3, 105.6	115.0, 54.8, 45.4
α, *β*, *γ* (°)	90.0, 102.0, 90.0	90.0, 90.0, 90.0	90.0, 101.2, 90.0	90.0, 90.0, 90.0	90.0, 101.4, 90.0
Resolution (Å) [1]	34.076–1.83 (1.90–1.83) [1]	46.77–2.14 (2.22–2.14) [1]	34.74–1.93 (2.11–1.93) [1]	47.11–2.14 (2.22–2.14) [1]	34.6–2.04 (2.11–2.04) [1]
R_{split}	1.45 (7.1)	0.83 (36.6)	0.94 (12.6)	0.75 (56.4)	0.81 (18.1)
CC1/2	0.980 (0.255)	0.995 (0.130)	0.990 (0.387)	0.996 (0.238)	0.993 (0.474)
I/σI	1.06	0.27	0.52	0.20	0.32
CC*	0.995 (0.949)	0.999 (0.480)	0.997 (0.747)	0.999 (0.620)	0.998 (0.802)
Completeness (%)	87.6 (0.56)	100.0 (100.0)	100.0 (100.0)	100.0 (99.0)	100.0 (100.0)
Redundancy	166	2378	400	310	497
Refinement					
Resolution (Å)	34.1–1.93 (1.99–1.93) [1]	46.8–2.1 (2.15–2.10) [1]	34.7–1.9 (1.95–1.90) [1]	47.1–2.17 (2.23–2.17) [1]	32.0–2.0 (2.05–2.00) [1]
No. reflections	17,608 (949)	45,326 (3045)	22,355 (1441)	41,092 (2971)	18,846 (1314)
R_{work}/R_{free}	0.21/0.26 (0.47/0.57)	0.23/0.24 (0.49/0.46)	0.21/0.25 (0.32/0.36)	0.23/0.27 (0.44/0.45)	0.23/0.27 (0.46/0.47)
No. atoms					
Protein	2439	4662	2447	4710	2447
Ligand/Ion/Water	112	104	55	79	40
B-factors					
Protein	45.68	58.42	44.43	57.56	49.02
Ligand/Ion/Water	51.48	57.40	43.69	52.70	46.00
Coordinate errors	0.37	0.35	0.29	0.38	0.37
R.m.s deviations					
Bond lengths (Å)	0.005	0.011	0.005	0.004	0.003
Bond angles (°)	0.746	1.535	0.744	0.907	0.635
Ramachandran plot					
Favored (%)	293 (96.4)	574 (62.5)	299 (98.4)	571 (96.5)	296 (97.4)
Allowed (%)	7 (2.3)	15 (2.5)	3 (1.0)	15 (2.6)	5 (1.6)
Disallowed (%)	4 (1.3)	6 (1.0)	2 (0.7)	6 (1.0)	3 (1.0)
Dataset	**Mpro14**	**Mpro16**	**Mpro17**	**Mpro18**	**Mpro19**
PDB ID	7VJW	7CWC	7VK7	7VJX	7VK6
Data collection [1]					
Beamline	LCLS (MFX)	LCLS (MFX)	LCLS (MFX)	LCLS (MFX)	LCLS (MFX)
Space group	P212121	P212121	P212121	P212121	P212121
Cell dimensions					
a, *b*, *c* (Å)	69.1, 104.1, 105.5	69.2, 104.3, 105.6	69.1, 104.3, 105.5	69.2, 104.3, 105.7	104.3, 105.5, 69.1
α, *β*, *γ* (°)	90.0, 90.0, 90.0	90.0, 90.0, 90.0	90.0, 90.0, 90.0	90.0, 90.0, 90.0	90.0, 90.0, 90.0
Resolution (Å) 1	34.55–2.34 (2.43–2.34) [1]	75.0–2.1 (2.14–2.10) [1]	41.93–2.24 (2.32–2.24) [1]	46.77–2.14 (2.22–2.14) [1]	16.82–2.14 (2.22–2.14) [1]
R_{split}	1.54 (8.3)	0.59 (3.33)	0.84 (2.3)	0.61 (−498.4)	1.03 (165.7)
CC1/2	0.979 (0.217)	0.997 (0.634)	0.995 (0.793)	0.997 (0.384)	0.993 (0.121)
I/σI	1.29	0.33	5.25	−0.02	0.08

Table 2. *Cont.*

Dataset	Mpro14	Mpro16	Mpro17	Mpro18	Mpro19
CC*	0.995 (0.649)	0.999 (0.678)	0.999 (0.941)	0.999 (0.509)	0.998 (0.465)
Completeness (%)	100.0 (100.0)	100.0 (100.0)	100.0 (100.0)	100.0 (96.0)	100.0 (100.0)
Redundancy	449	3105 (2025)	4683	4516	2370
Refinement					
Resolution (Å)	34.6–2.2 (2.25–2.20) [1]	42.0–2.1 (2.15–2.10) [1]	41.9–2.4 (2.48–2.40) [1]	46.8–2.2 (2.26–2.20) [1]	16.8–2.25 (2.39–2.25) [1]
No. reflections	39,287 (2628)	45,238 (3044)	30,465 (2599)	39,396 (2558)	36,768 (5902)
R_{work}/R_{free}	0.22/0.28 (0.37/0.39)	0.22/0.26 (0.37/0.44)	0.21/0.24 (0.34/0.36)	0.25/0.28 (0.37/0.37)	0.23/0.27 (0.37/0.38)
No. atoms					
Protein	4691	4710	4711	4710	4695
Ligand/Ion/Water	63	166	61	97	103
B-factors					
Protein	56.07	65.66	77.72	62.20	60.48
Ligand/Ion/Water	56.04	73.9	72.10	55.62	56.41
Coordinate errors	0.40	0.34	0.37	0.39	0.42
R.m.s deviations					
Bond lengths (Å)	0.008	0.003	0.002	0.001	0.002
Bond angles (°)	0.935	0.619	0.466	0.401	0.494
Ramachandran plot					
Favored (%)	568 (95.5)	580 (97.5)	571 (96.0)	571 (96.0)	576 (96.8)
Allowed (%)	23 (3.9)	14 (2.4)	19 (3.2)	22 (3.7)	16 (2.7)
Disallowed (%)	4 (0.7)	1 (0.1)	5 (0.8)	2 (0.3)	3 (0.5)

[1] The highest resolution shell is shown in parenthesis.

3. Results

3.1. Serial Crystallography Based Faster High-Throughput Drug Screening at an XFEL

During our LCLS beamtime (ID: mfx17318), the new-generation detector ePix10k2M was employed in dynamic gain mode. The new hybrid pixel detector ePix10k2M runs at repetition rates of 120 Hz up to 1 kHz, which allows much faster data acquisition rates compared to its predecessors [34]. During data collection, we did not experience any blockages with the MESH injector system. As a result, a total of 11,304,510 detector frames were collected in 1 day and 07 h 08 min with the new detector from Mpro microcrystals. Fifteen datasets were collected from 15 crystal soaks of Mpro with various potential drug candidates. The Mpro03 datasets were collected in 5 h 20 min as it was an early dataset; however, the Mpro19 samples took 36 min in a total of three runs, as the process was optimized during the first two days of our MFX beamtime (Table 1).

3.2. Determining Mpro Structures with Mitigated Radiation Damage at Near Physiological Temperature

A total of 17 samples were screened within the scope of the study. Two of these samples contained the drug-free apo Mpro protein crystals, while the other samples contained drug-soaked protein crystals. Full datasets were collected successfully for 15 of 17 samples. Two crystal slurry samples containing native Mpro crystals soaked with montelukast and ebselen displayed high amounts of precipitation and did not show any diffraction. Analysis of the remaining 15 samples from the collected diffraction data displayed resolution ranging from 1.90 Å to 2.4 Å. In addition, the electron densities belonging to the amino acid side chains forming the catalytic cavity are well-defined (Figure 1). This region is one of the most attractive target sites for drug repurposing studies. Moreover, the critical coordinated water molecules for catalytic activity, located between His41, Cys145, His164, and Asp187 from the active site [17], were observed in 8 of 15 structures after an initial refinement process (Figure 1).

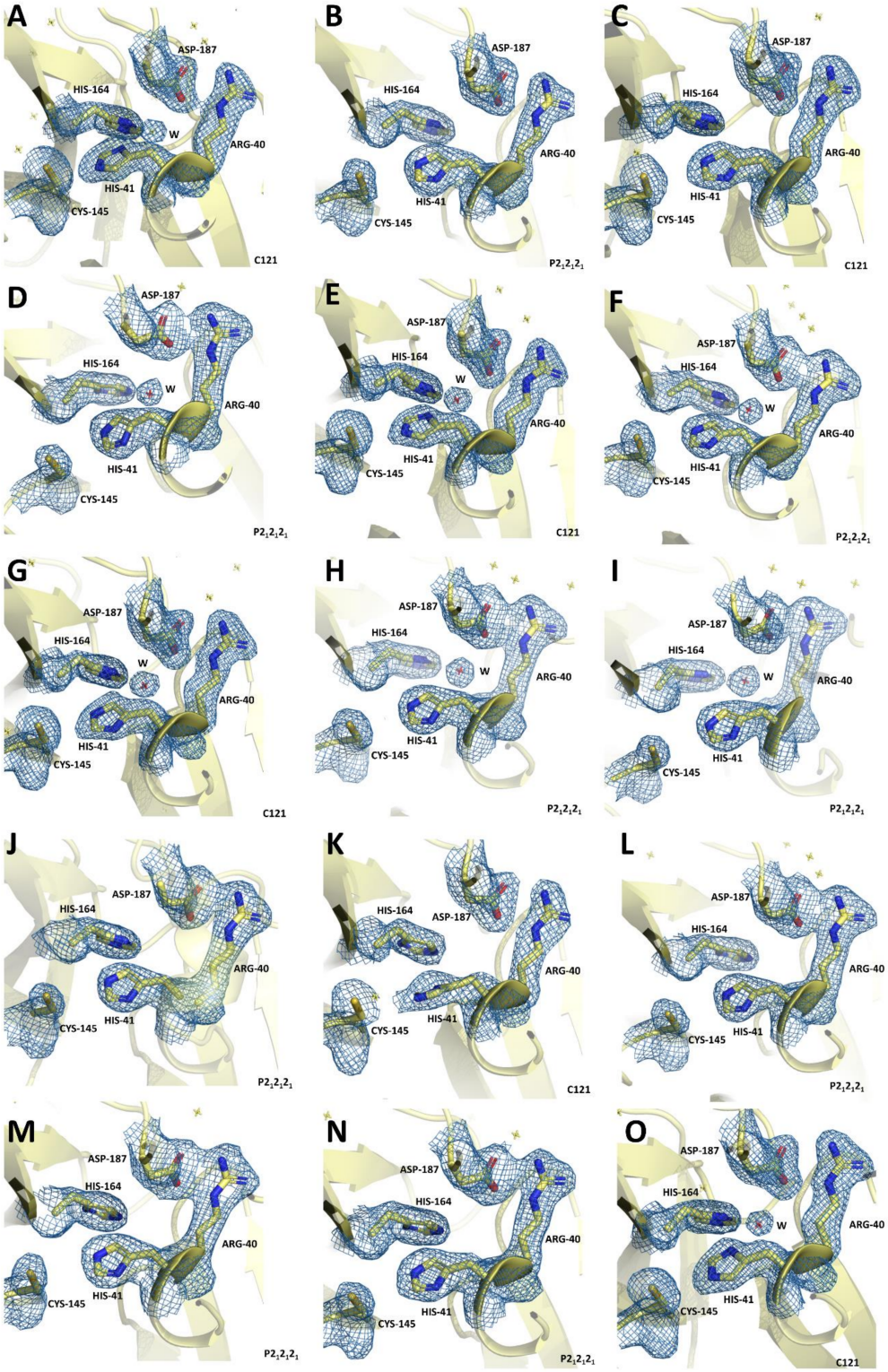


Figure 1. Electron density omit maps belonging to residues Arg40, His41, Cys145, His164, and Asp187 of SARS-CoV-2 Mpro structures. 2*Fo*-*Fc* simulated annealing-omit map is colored in slate and shown at 1.0σ level. Carbon atoms of Mpro are colored in yellow, nitrogen and oxygen atoms are colored by sky blue, and red, respectively. Space groups are shown in the bottom-right corner for each structure. Coordinated water molecules are indicated as "W". (**A**) Mpro9, (**B**) Mpro19, (**C**) Mpro13, (**D**) Mpro14, (**E**) Mpro 5, (**F**) Mpro16, (**G**) Mpro3, (**H**) Mpro10, (**I**) Mpro18, (**J**) Mpro6, (**K**) Mpro7, (**L**) Mpro12, (**M**) Mpro17, (**N**) Mpro 4, (**O**) Mpro11.

Despite these highly efficient and consistent results, target drugs could not be detected in any of the protein models after soaking at our standard 100 µg/mL concentration. Furthermore, ebselen- and montelukast-soaked crystals lost their ability to diffract in one of the two crystal forms. Precipitation in these crystal samples soaked with these two drugs may also occur as a result of binding or allosteric conformational changes. For ebselen and montelukast, cell-based and animal drug testing may provide more robust and detailed results. This is further explained in the discussion section.

3.3. Interpretation of Experimental Findings

Results are categorized under two space groups. The first space group (C121) includes six structures, while the second group ($P2_12_12_1$) includes nine. The structures were aligned (Figure 2) within their respective space groups, and the RMSD values were calculated (Tables 3 and 4). These RMSD values are indications of the similarity of refined structures, a lower RMSD indicates greater similarity. The highest RMSD value (0.54) is seen between the Mpro03 and Mpro07 structures. On the other hand, the lowest RMSD value (0.13) is observed between Mpro04 and Mpro10. All the structures in their respective space groups share the same sequence. Figure 2 shows that most conformational alterations occur at the loop region, which was expected. The helices and barrels are structurally conserved among the determined structures. The results of the data refinement process are indicated in Table 2. Ramachandran plot values in Table 2 show the percentage of residues in favorable and possible positions and outliers.

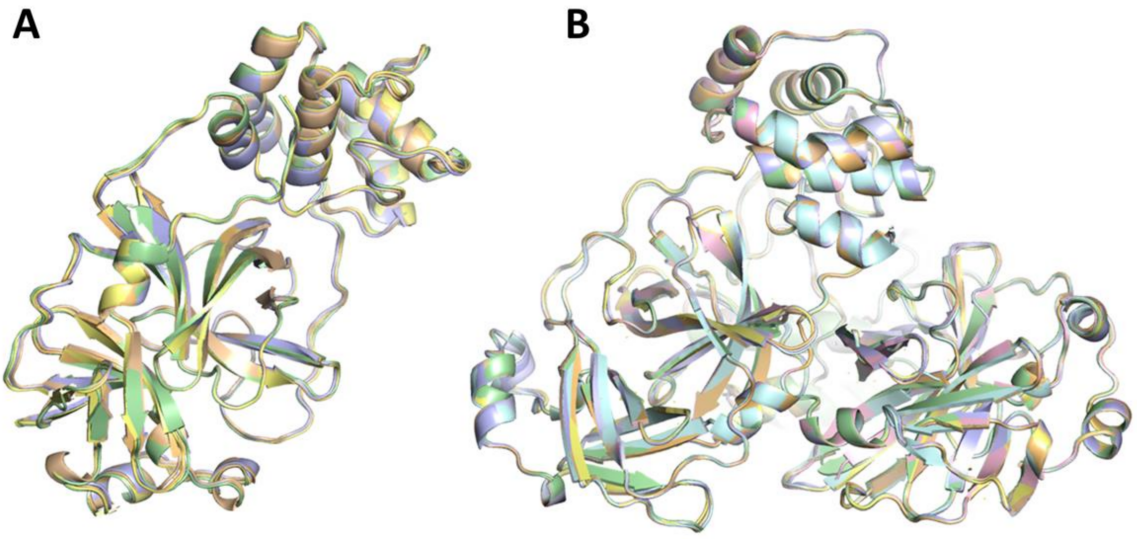


Figure 2. (**A**) Structural alignment of Mpro03, Mpro07, Mpro09, Mpro11, and Mpro13, all possessing similar cell constant values. Mpro03 is shown in wheat, Mpro07 in pale green, Mpro09 in light blue, Mpro11 in pale yellow, Mpro13 in light orange. RMSD values of alignments are given in Table 3. (**B**) Structural alignment of Mpro04, Mpro06, Mpro10, Mpro12, Mpro14, Mpro17, Mpro18, and Mpro19, all possessing similar cell constant values. Mpro04 is shown in wheat, Mpro06 in pale green, Mpro10 in light blue, Mpro12 in pale yellow, Mpro14 in light pink, Mpro17 in pale cyan, Mpro18 in light orange, Mpro19 in blue-white. RMSD values of alignments are given in Table 4.

Table 3. RMSD values of corresponding alignments within the C121 space group. ("-" symbol is added to avoid duplication of numbers).

	Mpro03	**Mpro07**	**Mpro09**	**Mpro11**
Mpro07	0.543	-	-	-
Mpro09	0.130	0.517	-	-
Mpro11	0.484	0.266	0.456	-
Mpro13	0.347	0.267	0.336	0.176

Table 4. RMSD values of corresponding alignments within the $P2_12_12_1$ space group. ("-" symbol is added to avoid duplication of numbers).

	Mpro04	**Mpro06**	**Mpro10**	**Mpro12**	**Mpro14**	**Mpro17**	**Mpro18**
Mpro06	0.184	-	-	-	-	-	-
Mpro10	0.132	0.183	-	-	-	-	-
Mpro12	0.134	0.165	0.142	-	-	-	-
Mpro14	0.154	0.138	0.153	0.154	-	-	-
Mpro17	0.201	0.192	0.182	0.184	0.175	-	-
Mpro18	0.160	0.182	0.144	0.156	0.145	0.161	-
Mpro19	0.1180	0.187	0.172	0.168	0.158	0.157	0.137

4. Discussion

To date, the number of high-throughput data collection for drug repurposing studies conducted at XFEL is limited. There are two main reasons: the low number of XFEL facilities, and time inefficiency when compared to other light sources. Two key elements determining XFEL data acquisition rate include detector technologies and pulses per second. Thanks to the next generation detector used in this study, a high dynamic range with low-noise diffraction patterns are obtained at 120 snapshots per second, six times increase over the previous detector installed at the MFX instrument. Such advances will shorten the timeframe of high-throughput drug screenings at XFELs and make them more feasible.

The results here shown indicate that no correlation exists between effective run time and resolution. Although runtimes vary between each data collection, our final run (Mpro19) indicates that a single run can be made in as short as 36 min. Getting accustomed to beamline setup and usage through online or real time data processing can help research groups use their beamtime more efficiently and allow for further high-throughput data collection.

In principle, co-crystallization and soaking are two common strategies for collecting diffraction data from protein–drug complex structures [43]. The soaking method involves "soaking" the protein crystal in the drug solution at a determined concentration, whereas co-crystallization mixes the drug and the target protein prior to crystallization. Among the two techniques, co-crystallization is the least preferred because it requires additional screening time, resources, and has unpredictable crystallization success rates. The soaking method is more cost-effective and allows multiple candidate drugs to be soaked into the crystals in a short time. However, the crystal packing may not be suitable for soaking, negatively impacting ligand binding to the target site. As a result, the success rate of drug binding depends upon various crystallographic parameters and is case-specific. To overcome this limitation, we performed our soaking experiments with two different crystal forms to increase the likelihood of drug binding. Despite our attempts, we obtained structural results with only subtle differences in the active site during the HTS process. Co-crystallization, used as an alternative method, may provide more accurate structural data to demonstrate the interaction between Mpro and, not only montelukast and ebselen, but also the other drug candidates.

In this study, nine drug candidates were screened for binding in two different crystal forms. However, none of the samples displayed noticeable experimental electron densities, suggesting at 100 µg/mL concentration soaking experiments failed. Interestingly, a high amount of precipitation was observed in two drug–protein samples containing montelukast and ebselen. Montelukast is a selective leukotriene receptor antagonist and an FDA-approved drug used in the treatment of chronic and prophylactic asthma [17]. Previously, montelukast was observed to have immunomodulatory and antiviral activities against dengue and ZIKA viruses. Therefore, it was hypothesized that montelukast may also have antiviral activity against SARS-CoV-2 [27]. Studies related to SARS-CoV-2-montelukast interaction are mostly in silico- [43–45] and in vitro- [17,42] oriented. Accordingly, we suggest that although montelukast interacts with Mpro, because of the limitations on the soaking experiments and/or used drug concentrations in the current study, we could not receive noticeable electron densities. Furthermore, observed precipitation for the Mpro-montelukast sample supports potential inhibitory effect of the montelukast.

In our study, we observed that ebselen-soaked $P2_12_12_1$ Mpro crystals did not provide any diffraction. Similar results were demonstrated by Malla et al. [46]. Ebselen is an organoselenium molecule that displays neuroprotective, anti-microbial, and anti-inflammatory effects by forming a selenosulfide bond with the thiol groups of cysteine residues in the relevant protein [47]. Ebselen has been proven to be a potent inhibitor of SARS-CoV-2 Mpro through HTS studies [47,48]. Not only in silico studies [49,50] but also in crystallographic studies [48] it has been shown that ebselen can bind to the relevant region of the Mpro. Accordingly, studies on the effect of ebselen on Mpro crystals support the precipitation we observed in our Mpro-ebselen sample, and hence the potential inhibitor effect of ebselen on SARS-CoV-2. Consequently, it is likely that these two drugs interact with Mpro.

5. Conclusions

De novo drug design and discoveries require exceptionally long lead times; nevertheless, structural high-throughput data collection for drug repurposing against new emerging diseases will be one of the fastest and most effective solutions. The recent advances in XFELs and detector technologies enable structural high-throughput drug screening. In this study, we performed high-throughput SFX data collection from nine different FDA-approved drugs soaked with the two different SARS-CoV-2 main protease Mpro crystal forms. The results of our soaking experiments performed at 100 μg/mL confirmed that none of the screened drugs displayed binding to Mpro at this concentration. It is essential to perform either the soaking experiments at higher drug concentrations, or further studies with cocrystallization are required to understand the effect of candidate drugs on Mpro.

Author Contributions: H.D. designed the experiment, H.D. performed the protein expression, purification. H.D., F.B.E. and O.G. (Omur Guven) performed the crystal screening. H.D., F.B.E., O.G. (Omur Guven), O.G. (Oktay Gocenler), C.B., E.A., S.B., G.K., Z.S., B.H., F.P., A.B., C.H.Y., R.G.S. and C.K. performed the remote data collection. The manuscript was prepared by H.D., O.G. (Omur Guven), F.B.E., B.C., E.A., B.Y., M.G., O.G. (Oktay Gocenler), C.B., G.U., N.T., S.D., J.A.J. and C.H.Y. All authors have read and agreed to the published version of the manuscript.

Funding: H.D. acknowledges support from National Science Foundation (NSF) Science and Technology Centers grant NSF-1231306 (Biology with X-ray Lasers, BioXFEL). This publication has been produced benefiting from the 2232 International Fellowship for Outstanding Researchers Program, the 2244 Industrial PhD Fellowship Program, and the 1001 Scientific and Technological Research Projects Funding Program of the Scientific and Technological Research Council of Turkey (TÜBİTAK) (Project Numbers: 118C270, 119C132 and 120Z520). However, the entire responsibility of the publication belongs to the owner of the publication. The financial support received from TÜBİTAK does not mean that the content of the publication is approved in a scientific sense by TÜBİTAK. Use of the LCLS, SLAC National Accelerator Laboratory, is supported by the U.S. Department of Energy, Office of Science, Office of Basic Energy Sciences under Contract No. DE-AC02-76SF00515.

Institutional Review Board Statement: Not applicable.

Informed Consent Statement: Not applicable.

Data Availability Statement: The 3D electron density map of SARS-CoV-2 Main protease has been deposited in the ProteinDataBank under accession numbers 7VJW (Lopinavir, $P2_12_12_1$), 7VJX (Rosuvastatin, $P2_12_12_1$), 7VJY (apo form, C121), 7VJZ (Adefovir, C121), 7VK0 (Umifenovir, $P2_12_12_1$), 7VK1 (Umifenovir, C121), 7VK2 (Lopinavir, C121), 7VK3 (apo form, $P2_12_12_1$), 7VK4 (Montelukast,$P2_12_12_1$), 7VK5 (Adefovir,$P2_12_12_1$), 7VK6 (Empagliflozin, $P2_12_12_1$), 7VK7 (Atorvastatin,$P2_12_12_1$), and 7VK8 (Ebselen, C121). This paper does not report original code. Any additional information required to reanalyze the data reported is available from the lead contact upon request.

Acknowledgments: The authors gratefully acknowledge use of the services and facilities of the Koç University IsBank Infectious Disease Center (KUIS-CID). The authors gratefully acknowledge use of the services and facilities of the Koç University Research Center for Translational Medicine (KUTTAM), funded by the Presidency of Turkey, Presidency of Strategy and Budget. The content is solely the responsibility of the authors and does not necessarily represent the official views of the

Presidency of Strategy and Budget. H.D. would like to thank Michelle Young, Ritu Khurana, Lori Anne Love, and Tracy Chou for their invaluable support and discussions.

Conflicts of Interest: The authors declare no conflict of interest.

References

1. Morse, S.S. Factors in the emergence of infectious diseases. *Plagues Politics* **1995**, *1*, 7–15. [CrossRef] [PubMed]
2. Fauci, A.S.; Folkers, G.K. The world must build on three decades of scientific advances to enable a new generation to live free of HIV/AIDs. *Health Aff.* **2012**, *31*, 1529–1536. [CrossRef]
3. Steere, A.C.; Coburn, J.; Glickstein, L. The emergence of Lyme disease. *J. Clin. Investig.* **2004**, *113*, 1093–1101. [CrossRef] [PubMed]
4. Morens, D.M.; Taubenberger, J.K.; Fauci, A.S. The persistent legacy of the 1918 influenza virus. *N. Engl. J. Med.* **2009**, *361*, 225–229. [CrossRef]
5. Andersen, K.G.; Rambaut, A.; Lipkin, W.I.; Holmes, E.C.; Garry, R.F. The proximal origin of SARS-CoV-2. *Nat. Med.* **2020**, *26*, 450–452. [CrossRef]
6. Jones, K.E.; Patel, N.G.; Levy, M.A.; Storeygard, A.; Balk, D.; Gittleman, J.L.; Daszak, P. Global trends in emerging infectious diseases. *Nature* **2008**, *451*, 990–993. [CrossRef]
7. Qiao, J.; Li, Y.-S.; Zeng, R.; Liu, F.-L.; Luo, R.-H.; Huang, C.; Wang, Y.-F.; Zhang, J.; Quan, B.; Shen, C.; et al. SARS-CoV-2 mpro inhibitors with antiviral activity in a transgenic mouse model. *Science* **2021**, *371*, 1374–1378. [CrossRef] [PubMed]
8. Dai, W.; Zhang, B.; Jiang, X.-M.; Su, H.; Li, J.; Zhao, Y.; Xie, X.; Jin, Z.; Peng, J.; Liu, F.; et al. Structure-based design of antiviral drug candidates targeting the SARS-CoV-2 main protease. *Science* **2020**, *368*, 1331–1335. [CrossRef]
9. Li, Q.; Kang, C.B. Progress in developing inhibitors of SARS-CoV-2 3c-like protease. *Microorganisms* **2020**, *8*, 1250. [CrossRef] [PubMed]
10. Mengist, H.M.; Dilnessa, T.; Jin, T. Structural basis of potential inhibitors targeting SARS-CoV-2 main protease. *Front. Chem.* **2021**, *9*, 622898. [CrossRef] [PubMed]
11. Sacco, M.D.; Ma, C.; Lagarias, P.; Gao, A.; Townsend, J.A.; Meng, X.; Dube, P.; Zhang, X.; Hu, Y.; Kitamura, N.; et al. Structure and inhibition of the SARS-CoV-2 main protease reveal strategy for developing dual inhibitors against M^{pro} and cathepsin L. *Sci. Adv.* **2020**, *6*, eabe0751. [CrossRef] [PubMed]
12. Ullrich, S.; Nitsche, C. The SARS-CoV-2 main protease as drug target. *Bioorg. Med. Chem. Lett.* **2020**, *30*, 127377. [CrossRef] [PubMed]
13. Mahase, E. COVID-19: Pfizer's paxlovid is 89% effective in patients at risk of serious illness, company reports. *BMJ* **2021**, *375*, n2697. [CrossRef] [PubMed]
14. Zhang, L.; Lin, D.; Kusov, Y.; Nian, Y.; Ma, Q.; Wang, J.; von Brunn, A.; Leyssen, P.; Lanko, K.; Neyts, J.; et al. α-Ketoamides as broad-spectrum inhibitors of coronavirus and enterovirus replication: Structure-based design, synthesis, and activity. *J. Med. Chem.* **2020**, *63*, 4562–4578. [CrossRef] [PubMed]
15. Pillaiyar, T.; Manickam, M.; Namasivayam, V.; Hayashi, Y.; Jung, S.-H. An overview of severe acute respiratory syndrome–coronavirus (SARS-CoV) 3CL protease inhibitors: Peptidomimetics and small molecule chemotherapy. *J. Med. Chem.* **2016**, *59*, 6595–6628. [CrossRef] [PubMed]
16. Huang, N.; Deng, H.; Liu, B.; Wang, D.; Zhao, Z. Features and futures of X-ray free-electron lasers. *Innovation* **2021**, *2*, 100097. [CrossRef]
17. Durdagi, S.; Dag, Ç.; Dogan, B.; Sierra, R.; Snell, E.; DeMirci, H. Near-physiological-temperature serial crystallography reveals conformations of SARS-CoV-2 main protease active site for improved drug repurposing. *Structure* **2021**, *29*, 1–15. [CrossRef]
18. Blay, V.; Tolani, B.; Ho, S.P.; Arkin, M.R. High-throughput screening: Today's biochemical and cell-based approaches. *Drug Discov. Today* **2020**, *25*, 1807–1821. [CrossRef]
19. Aceti, D.J.; Ahmed, H.; Westler, W.M.; Wu, C.; Dashti, H.; Tonelli, M.; Eghbalnia, H.; Amarasinghe, G.K.; Markley, J.L. Fragment screening targeting Ebola virus nucleoprotein C-terminal domain identifies lead candidates. *Antivir. Res.* **2020**, *180*, 104822. [CrossRef] [PubMed]
20. Aretz, J.; Baukmann, H.; Shanina, E.; Hanske, J.; Wawrzinek, R.; Zapol'skii, V.A.; Seeberger, P.H.; Kaufmann, D.E.; Rademacher, C. Identification of multiple druggable secondary sites by fragment screening against DC-SIGN. *Angew. Chem. Int. Ed.* **2017**, *56*, 7292–7296. [CrossRef]
21. Schuller, M.; Correy, G.J.; Gahbauer, S.; Fearon, D.; Wu, T.; Díaz, R.E.; Young, I.D.; Carvalho Martins, L.; Smith, D.H.; Schulze-Gahmen, U.; et al. Fragment binding to the nsp3 macrodomain of SARS-COV-2 identified through crystallographic screening and computational docking. *Sci. Adv.* **2021**, *7*, eabf8711. [CrossRef]
22. Gupta, S.; Singh, A.K.; Kushwaha, P.P.; Prajapati, K.S.; Shuaib, M.; Senapati, S.; Kumar, S. Identification of potential natural inhibitors of SARS-CoV2 main protease by molecular docking and Simulation Studies. *J. Biomol. Struct. Dyn.* **2020**, *39*, 4334–4345. [CrossRef] [PubMed]
23. Reiner, Ž.; Hatamipour, M.; Banach, M.; Pirro, M.; Al-Rasadi, K.; Jamialahmadi, T.; Radenkovic, D.; Montecucco, F.; Sahebkar, A. Statins and the COVID-19 main protease: In silico evidence on direct interaction. *Arch. Med. Sci.* **2020**, *16*, 490–496. [CrossRef]
24. Dhote, A.M.; Patil, V.R.; Lokwani, D.K.; Amnerkar, N.D.; Ugale, V.G.; Charbe, N.B.; Bhongade, B.A.; Khadse, S.C. Strategic analyses to identify key structural features of antiviral/antimalarial compounds for their binding interactions with 3CLpro, PLpro and RdRp of SARS-CoV-2: In silico molecular docking and dynamic simulation studies. *J. Biomol. Struct. Dyn.* **2021**, 1–18. [CrossRef] [PubMed]

25. Choudhary, S.; Silakari, O. Scaffold morphing of arbidol (umifenovir) in search of multi-targeting therapy halting the interaction of SARS-CoV-2 with ACE2 and other proteases involved in COVID-19. *Virus Res.* **2020**, *289*, 198146. [CrossRef]
26. Ekins, S.; Mottin, M.; Ramos, P.R.P.S.; Sousa, B.K.P.; Neves, B.J.; Foil, D.H.; Zorn, K.M.; Braga, R.C.; Coffee, M.; Southan, C.; et al. Déjà Vu: Stimulating open drug discovery for SARS-CoV-2. *Drug Discov. Today* **2020**, *25*, 928–941. [CrossRef]
27. Copertino, D.C.; Duarte, R.R.; Powell, T.R.; Mulder Rougvie, M.; Nixon, D.F. Montelukast drug activity and potential against severe acute respiratory syndrome coronavirus 2 (SARS-CoV-2). *J. Med. Virol.* **2020**, *93*, 187–189. [CrossRef]
28. Durdagi, S.; Avsar, T.; Orhan, M.D.; Serhatli, M.; Balcioglu, B.K.; Ozturk, H.U.; Kayabolen, A.; Cetin, Y.; Aydinlik, S.; Bagci-Onder, T.; et al. The neutralization effect of montelukast on SARS-CoV-2 is shown by multiscale in silico simulations and combined in vitro studies. *Mol. Ther.* **2021**, in press. [CrossRef]
29. Sierra, R.G.; Laksmono, H.; Kern, J.; Tran, R.; Hattne, J.; Alonso-Mori, R.; Lassalle-Kaiser, B.; Glöckner, C.; Hellmich, J.; Schafer, D.W.; et al. Nanoflow electrospinning serial femtosecond crystallography. *Acta Crystallogr. Sect. D Struct. Biol.* **2012**, *68*, 1584–1587. [CrossRef]
30. Sierra, R.G.; Gati, C.; Laksmono, H.; Dao, E.H.; Gul, S.; Fuller, F.; Kern, J.; Chatterjee, R.; Ibrahim, M.; Brewster, A.S.; et al. Concentric-flow electrokinetic injector enables serial crystallography of ribosome and photosystem II. *Nat. Methods* **2015**, *13*, 59–62. [CrossRef] [PubMed]
31. Mariani, V.; Morgan, A.; Yoon, C.H.; Lane, T.J.; White, T.A.; O'Grady, C.; Kuhn, M.; Aplin, S.; Koglin, J.; Barty, A.; et al. OnDA: Online data analysis and feedback for serial X-ray imaging. *J. Appl. Cryst.* **2016**, *49*, 1073–1080. [CrossRef] [PubMed]
32. Damiani, D.; Dubrovin, M.; Gaponenko, I.; Kroeger, W.; Lane, T.J.; Mitra, A.; O'Grady, C.P.; Salnikov, A.; Sanchez-Gonzalez, A.; Schneider, D.; et al. Linac coherent light source data analysis using psana. *J. Appl. Cryst.* **2016**, *49*, 672–679. [CrossRef]
33. Thayer, J.; Damiani, D.; Ford, C.; Dubrovin, M.; Gaponenko, I.; O'Grady, C.P.; Kroeger, W.; Pines, J.; Lane, T.J.; Salnikov, A.; et al. Data systems for the linac coherent light source. *Adv. Struct. Chem. Imag.* **2017**, *3*, 1–13. [CrossRef] [PubMed]
34. Van Driel, T.B.; Nelson, S.; Armenta, R.; Blaj, G.; Boo, S.; Boutet, S.; Doering, D.; Dragone, A.; Hart, P.; Haller, G.; et al. The epix10k 2-megapixel hard X-ray detector at LCLS. *J. Synchrotron Radiat.* **2020**, *27*, 608–615. [CrossRef]
35. Barty, A.; Kirian, R.A.; Maia, F.R.; Hantke, M.; Yoon, C.H.; White, T.A.; Chapman, H. Cheetah: Software for high-throughput reduction and analysis of serial femtosecond X-ray diffraction data. *J. Appl. Cryst.* **2014**, *47*, 1118–1131. [CrossRef]
36. White, T.A.; Kirian, R.A.; Martin, A.V.; Aquila, A.; Nass, K.; Barty, A.; Chapman, H.N. CrystFEL: A software suite for snapshot serial crystallography. *J. Appl. Cryst.* **2012**, *45*, 335–341. [CrossRef]
37. White, T.A.; Mariani, V.; Brehm, W.; Yefanov, O.; Barty, A.; Beyerlein, K.R.; Chervinskii, F.; Galli, L.; Gati, C.; Nakane, T.; et al. Recent developments in CrystFEL. *J. Appl. Cryst.* **2016**, *49*, 680–689. [CrossRef]
38. Winn, M.D. Overview of the CCP4 suite and current developments. *Acta Crystallogr. Sect. D Struct. Biol.* **2011**. [CrossRef]
39. McCoy, A.J.; Grosse-Kunstleve, R.W.; Adams, P.D.; Winn, M.D.; Storoni, L.C.; Read, R.J. Phaser crystallographic software. *J. Appl. Cryst.* **2007**, *40*, 658–678. [CrossRef] [PubMed]
40. Adams, P.D.; Afonine, P.V.; Bunkóczi, G.; Chen, V.B.; Davis, I.W.; Echols, N.; Headd, J.J.; Hung, L.W.; Kapral, G.J.; Grosse-Kunstleve, R.W.; et al. PHENIX: A comprehensive Python-based system for macromolecular structure solution. *Acta Crystallogr. Sect. D Biol. Crystallogr.* **2010**, *66*, 213–221. [CrossRef] [PubMed]
41. Emsley, P.; Cowtan, K. Coot: Model-building tools for molecular graphics. *Acta Crystallogr. Sect. D Biol. Crystallogr.* **2004**, *60*, 2126–2132. [CrossRef] [PubMed]
42. DeLano, W. Pymol. In *The PyMOL Molecular Graphics System, Version*; Schrödinger, LLC: New York, NY, USA, 2020; Volume 2.
43. Wienen-Schmidt, B.; Oebbeke, M.; Ngo, K.; Heine, A.; Klebe, G. Two methods, one goal: Structural differences between cocrystallization and crystal soaking to discover ligand binding poses. *ChemMedChem* **2020**, *16*, 292–300. [CrossRef]
44. Mansoor, S.; Saadat, S.; Amin, A.; Ali, I.; Ghaffar, M.T.; Amin, U.; Mukhtar, M. A case for montelukast in COVID-19: "The use of computational docking to estimate the effects of montelukast on potential viral main protease catalytic site". *Res. Sq.* **2020**. [CrossRef]
45. Watashi, K. Identifying and repurposing antiviral drugs against severe acute respiratory syndrome coronavirus 2 with in silico and in vitro approaches. *Biochem. Biophys. Res. Commun.* **2021**, *538*, 137–144. [CrossRef] [PubMed]
46. Malla, T.N.; Pandey, S.; Poudyal, I.; Feliz, D.; Noda, M.; Phillips, G.; Stojkovic, E.; Schmidt, M. Ebselen Reacts with SARS Coronavirus-2 Main Protease Crystals. *bioRxiv* **2020**. [CrossRef]
47. Ma, C.; Hu, Y.; Townsend, J.A.; Lagarias, P.I.; Marty, M.T.; Kolocouris, A.; Wang, J. Ebselen, disulfiram, carmofur, PX-12, tideglusib, and shikonin are nonspecific promiscuous SARS-CoV-2 main protease inhibitors. *ACS Pharmacol. Transl. Sci.* **2020**, *3*, 1265–1277. [CrossRef]
48. Amporndanai, K.; Meng, X.; Shang, W.; Jin, Z.; Rogers, M.; Zhao, Y.; Rao, Z.; Liu, Z.-J.; Yang, H.; Zhang, L.; et al. Inhibition Mechanism of SARS-CoV-2 Main Protease by Ebselen and Its Derivatives. *Nat. Commun.* **2021**, *12*, 3061. [CrossRef]
49. Nogara, P.A.; Omage, F.B.; Bolzan, G.R.; Delgado, C.P.; Aschner, M.; Orian, L.; Teixeira Rocha, J.B. In silico studies on the interaction between Mpro and PLpro from SARS-CoV-2 and Ebselen, its metabolites and derivatives. *Mol. Inform.* **2021**, *40*, 2100028. [CrossRef]
50. Jin, Z.; Du, X.; Xu, Y.; Deng, Y.; Liu, M.; Zhao, Y.; Zhang, B.; Li, X.; Zhang, L.; Peng, C.; et al. Structure of Mpro from SARS-CoV-2 and discovery of Its inhibitors. *Nature* **2020**, *582*, 289–293. [CrossRef]